Holistic view on cation interdiffusion during processing and operation of garnet all-solid-state batteries

Kai Yao [a,b], Walter Sebastian Scheld [a], Qianli Ma [a], Yuan Zeng [a], Swapna Ganapathy [c], Martin Ihrig [a], Ruijie Ye [a], Meng Ma [d], Vivien Kiyek [a], Olivier Guillon [a,e,f], Mark Huijben [g], Johan E. ten Elshof [g], Martin Finsterbusch [a,e], Dina Fattakhova-Rohlfing [a,b,e,*]

[a] *Forschungszentrum Jülich GmbH, Institute of Energy Materials and Devices: Materials Synthesis and Processing (IMD-2), Wilhelm-Johnen-Straße, 52428 Jülich, Germany*
[b] *University Duisburg-Essen, Faculty of Engineering and Center for Nanointegration Duisburg-Essen CENIDE, Lotharstraße 1, 47057 Duisburg, Germany*
[c] *Delft University of Technology, Mekelweg 5, 2628 CD Delft, the Netherlands*
[d] *Frontiers Science Center for Flexible Electronics, Xi'an Institute of Flexible Electronics and Xi'an Institute of Biomedical Materials & Engineering, Northwestern Polytechnical University, Xi'an 710072, PR China*
[e] *Helmholtz Institute Münster: Ionics in Energy Storage (IEK-12), Forschungszentrum Jülich GmbH, Corrensstr. 46, 48149 Münster, Germany*
[f] *Jülich-Aachen Research Alliance: JARA-Energy, 52425, Jülich, Germany*
[g] *MESA+ Institute for Nanotechnology, University of Twente, PO Box 217, 7500 AE Enschede, the Netherlands*

ARTICLE INFO

ABSTRACT

All-solid-state batteries based on the active cathode material LiCoO$_2$ (LCO), a garnet-type Li$_7$La$_3$Zr$_2$O$_{12}$ (LLZO) electrolyte and a Li-metal anode are attracting a lot of attention as a robust and safe alternative to conventional lithium-ion batteries. The challenges in the practical realization of such cells are related to high-temperature sintering, which compacts the ceramic powder but also leads to undesirable material interactions such as cation interdiffusion and secondary phase formation. Even if high initial capacities can be achieved, the all-inorganic cells suffer from a strong capacity drop due to various degradation phenomena during processing and operation, which are not yet fully understood. In this study, the thermodynamic and kinetic aspects of co-sintering as well as the structural evolution of materials and interfaces during processing and operation of co-sintered LCO-LLZO cathodes are investigated in detail. A thermodynamic model for the interdiffusion of cations is derived and the effects of the diffusion of Al- and Co-ions, which occurs during the processing and cycling of the cells, are investigated. In LLZO, the diffusion of 0.13 Co per formula unit (*pfu*) has a negligible effect on ionic and electronic conductivity and electrochemical stability. In contrast, the substitution of 0.01 *pfu* Al and the induced disorder in the layer structure of LCO increases the polarization during cycling. All-inorganic cells fabricated with optimized sintering parameters to minimize interdiffusion between LCO and LLZO show good initial performance but similar degradation during cycling, as the used processing parameters result in a more porous microstructure leading to the development of cracks along the LLZO/LCO interface. The results obtained highlight the inherent instabilities of all-ceramic cathodes with unprotected LCO/LLZO interfaces, which require precise tuning of materials and processing parameters to achieve both high mechanical stability and low interdiffusion.

1. Introduction

Since the commercialization of Li-ion batteries, the continuous development for higher energy density and enhanced safety has been an ongoing endeavor. Replacing liquid electrolytes with solid electrolytes is widely regarded as one of the most promising possibilities to achieve these goals [1-3]. Among various solid-state Li-ion conductors, garnet-type Li$_7$La$_3$Zr$_2$O$_{12}$ (commonly known as LLZO) substituted with various ions (mainly Al, Ta, Ga and Nb) has received much attention in recent years due to its relatively high ionic conductivity (up to 2 mS cm^{-1} at room temperature), wide electrochemical stability window, excellent thermal stability and non-flammability [4,5]. One of the

unique properties of LLZO is its high stability towards Li metal, which makes it a very attractive separator and anolyte material for high energy cells with Li metal anode. The excellent performance of LLZO was recently demonstrated in symmetric cells with Li metal electrodes, for which critical current densities of up to 100 mA cm^{-2} were achieved without dendrite formation [6].

LLZO exhibits a high enough Li-ion conductivity to be also used as a catholyte, enabling fully inorganic all-solid-state batteries (ASSB) that do not contain flammable organic components and thus achieve the highest possible safety on cell level. However, in order to achieve the necessary high loading of cathode active material (CAM) required for obtaining high energy density, the morphology of positive electrodes in garnet-based cells should be similar to that of conventional lithium-ion batteries, where the electrolyte is infiltrated into a porous CAM matrix. The resulting composite electrodes with a percolating matrix of ion conducting material in the electrode enable rapid lithiation/de-lithiation of even thick cathodes, as most CAMs have low ionic conductivity [7].

The challenges in the practical realization of such cathode architectures in garnet-based cells are related to the fact that LLZO and most inorganic CAMs are solids with high elastic moduli (LLZO with more than 150 GPa [8,9] and for example LiCoO$_2$ (LCO) with 174 $\pm$ 25 GPa [10]), which requires sintering at elevated temperatures to establish contact between the particles with a sufficiently low interfacial impedance. However, as the sintering process is typically diffusion driven, it can also trigger a number of undesirable processes. It has long been known that the thermal stability of CAMs decreases significantly in the presence of LLZO with the formation of various reaction products [11, 12]. Among the numerous CAMs, LCO exhibits the highest thermal stability with LLZO and is so far the only known material that can be successfully sintered in combination with LLZO powders to form ceramic composite cathodes with good performance and without any sintering aids [13,14]. However, numerous material interactions can also take place in the LCO-LLZO system during sintering, which lead to material degradation during processing and impair the performance of the final cell. One of these processes is the interdiffusion of highly mobile ions such as Al (from Al-doped LLZO) and Co (from LCO) with the formation of substituted or doped phases [7,15]. In addition, reactions with the formation of various secondary phases such as Li$_{0.5}$La$_2$Co$_{0.5}$O$_4$ or Co-doped LLZO are frequently observed, leading to an additional loss in capacity [16,17]. Intensive research into the production of garnet-based composite cathodes has led to the optimization of their phase purity and a strong suppression of undesirable reactions during processing. However, even optimized cathodes show a strong capacity drop during battery operation. One of the well-documented mechanisms is the mechanical degradation during charge and discharge caused by the volume changes in the cathode material during lithiation/de-lithiation [18]. Another degradation process is related to the electrochemical stability of the interface, as highly mobile ions can interdiffuse under electric fields or due to changes in oxidation state of cathode active material [19]. Thus, it was recently reported that the interdiffusion of Al- and Co-ions at the interface occurs not only during processing but also during battery operation and is thermodynamically driven by the change in the oxidation state of LCO [20].

Understanding the processes that affect the electrochemical properties of all-solid-state LCO-LLZO composite cathodes is of paramount importance for developing strategies to improve their performance, which explains the ever-increasing number of publications on this topic. However, despite the knowledge gained in recent years, there are still many questions that need to be clarified. Although the interdiffusion of ions during processing is thought to be an important degradation mechanism, little is known about the structure and properties of the products formed and their potential impact on cell performance. Some current studies focus primarily on the effect of diffusion on the LLZO properties and neglect its effect on the LCO [16,17]. However, this knowledge is important for the development of optimization strategies,

both experimentally and theoretically. Comparison of the results reported by different groups is generally not straightforward because the conditions for cathode fabrication differ significantly and the criteria for comparing sintering conditions have not yet been developed. Furthermore, although individual degradation phenomena are studied in detail, much less is known about whether the individual contributions are interrelated and how they influence the overall degradation process. In particular, the relationship between the "processing history" of the cathodes (such as structure and properties of the processing-induced products or degree of interdiffusion) and electrochemically induced degradation during operation is important, as ceramic cathodes always need to be heat-treated during fabrication before they are assembled in the battery for electrochemically testing.

To clarify these questions, we have re-examined the processes that take place during the sintering of LCO and LLZO powders, with particular attention to the thermodynamic driving force of possible reactions. Based on the experimental results of the differential thermal analysis and the theoretical calculation of the free energy of reaction, we have defined the experimental conditions under which the formation of secondary phases can be excluded and ion interdiffusion can be considered as the only process at the interface between LCO and LLZO. We propose a simple model to estimate the degree of interdiffusion as a function of temperature and time, allowing a more rational choice of sintering parameters. Using this model, we selected sintering conditions that allow maximum interdiffusion without the formation of secondary phases, and used respective samples for analysis of their structure and electrochemical properties. Finally, we selected a new set of sintering parameters with minimized interdiffusion for LCO-LLZO full cells, which then were analyzed with respect to performance and degradation. Our results show that although the formation of secondary phases at the LCO-LLZO interfaces occurs, the interdiffusion of Co- and Al-ions between LCO and Al-doped LLZO cannot be completely avoided, as it always occurs at the temperatures practically relevant for powder sintering. Interdiffusion leads to a decrease in ionic conductivity and Li-ion mobility in both phases, which does not drastically deteriorate their performance in liquid electrolytes, but negatively affects the properties of the solid/solid interface, leading to a significant capacity drop already after first cycle. Furthermore, the specific sintering conditions to minimize interdiffusion negatively affect the mechanical properties of the resulting cell, leading to a continuous capacity drop due to mechanical failure. Our results elucidate the inherent instabilities of all-ceramic cathodes with unprotected LCO/LLZO interfaces, which necessitates accurate balancing of materials and processing parameters to achieve both high mechanical stability and low interdiffusion.

2. Results and discussion

Fabrication of ceramic LCO-LLZO cathodes from the corresponding powders inevitably involves a high-temperature sintering process, which is necessary to densify the powders. Numerous publications report that the temperature required for sintering LCO and LLZO powders in pure ceramic cathodes should be above 1000 °C, with around 1050 °C being used as the sintering temperature in most publications [7]. This is confirmed by numerous experimental observations, which show no formation of secondary phases [13,14,21]. However, theoretical calculations for this system were also conducted, revealing thermodynamic instability at 0 K [11,22]. At the same time, recent publications show that even in apparently phase-pure sintered cathodes, diffusion of mobile ions occurs at the interface, which has been observed experimentally by several groups but not yet studied in detail [13,16,17, 20].

To understand the thermally induced processes between LLZO and LCO in a wider temperature range, we investigated the thermodynamics of the processes using thermogravimetric analysis (TG) and differential thermal analysis (DTA), followed by X-ray diffraction analysis (XRD) of the reaction products. We also re-examined the theoretical energies of

formation of possible reaction products in the LCO-LLZO system.

The DTA and TG curves of the 50:50 wt% mixture of LLZO and LCO powders show several distinctly different regions (Fig. 1a). It can be observed that there is a slight mass loss (~0.079 %) at the beginning of heating from room temperature to 280 °C, which is due to the removal of moisture adsorbed on the powder surface. With increasing temperature, the mass starts to decrease rapidly at 415 °C and a broad peak can be observed in the DTA curve, reaching its maximum at 573 °C. This process is due to the decomposition of LiOH, which releases water [23]. Subsequently, from ~630 °C to ~1100 °C, the DTA increases steadily, accompanied by a continuous and linear mass loss (about 0.5 %) observed in the TG curve. At temperatures above 1100 °C, the DTA curve increases sharply, while the TG curve shows a significant mass loss of about 2 %. The results of the DTA and TG analyses indicate that the reaction between LLZO and LCO starts at 630 °C and apparently proceeds in two distinct stages, with a relatively slow reaction between 630 °C and 1100 °C (Stage 1) and a more intense reaction beyond 1100 °C (Stage 2).

The experimental thermodynamic results are strongly supported by theoretical calculations. We have calculated the Gibbs energy of the reaction between LLZO and LCO from the temperature where the reaction starts, which is 996 K (723 °C), to 1500 K (1227 °C) [11,22,24]. As shown in the pseudo-binary phase diagram (Fig. 1b), the absolute value of negative reaction Gibbs energy increases uniformly with increasing temperature, indicating that the reaction pathway remains essentially unchanged and only the relative amount of reaction products changes continuously. The steady increase of the corresponding formation energies up to 1400 K (1127 °C) agrees well with the steady increase in the DTA curves and with the results of the XRD analysis (Fig. 1c) in the same temperature range. The XRD patterns of the compressed powder

mixtures annealed for 2 h at temperatures up to 1000 °C show no formation of secondary phases. The observed reflections correspond exclusively to the patterns of the starting materials, even if their relative intensities change. This is particularly evident for the diffraction peak of LCO at 19.0°, which is discussed below. A possible explanation for the observed results is that the temperature-induced interactions between LLZO and LCO occur at temperatures below ~1400 K (1127 °C) via the formation of a metastable phase that is kinetically stable during the relatively short duration (typically less than 2 h) of the sintering process. Based on literature analysis [16] and our own experience [17], it can be hypothesized that these metastable phases result from the interdiffusion of ions (mainly Al dopant from LLZO and Co from LCO as experimentally observed by numerous groups), which are incorporated into the lattices of starting materials [16,25,26]. In the XRD patterns, no obvious evolution of lattice parameters and peak signals is observed with increasing temperature. This may be attributed to the small amount of diffused Co and the strong signal of LCO masking the signal of LLZO. A more detailed experimental analysis of the metastable phases formed, which confirms this hypothesis, is presented below.

Above 1400 K (1127 °C), there are clear differences in the calculated reaction energy between adjacent curves. In addition, at temperatures above 1410 K (1127 °C), a higher atomic fraction of LCO is involved in the reaction. This indicates an enhanced reaction in this temperature range, which is consistent with the results of TG-DTA measurements (the reaction equations are listed in Tab. S1) and the XRD analysis. Upon reaching 1100 °C, a new reflection at 23.4° appears in the XRD patterns, which is assigned to $LaCoO_3$ (PDF 48-0123). It is noteworthy that the critical temperature of 1400 K (1127 °C) resulting from the theoretical calculations is very close to the experimental value of 1100 °C [13,14, 27]. Below this critical temperature the reaction between the electrolyte
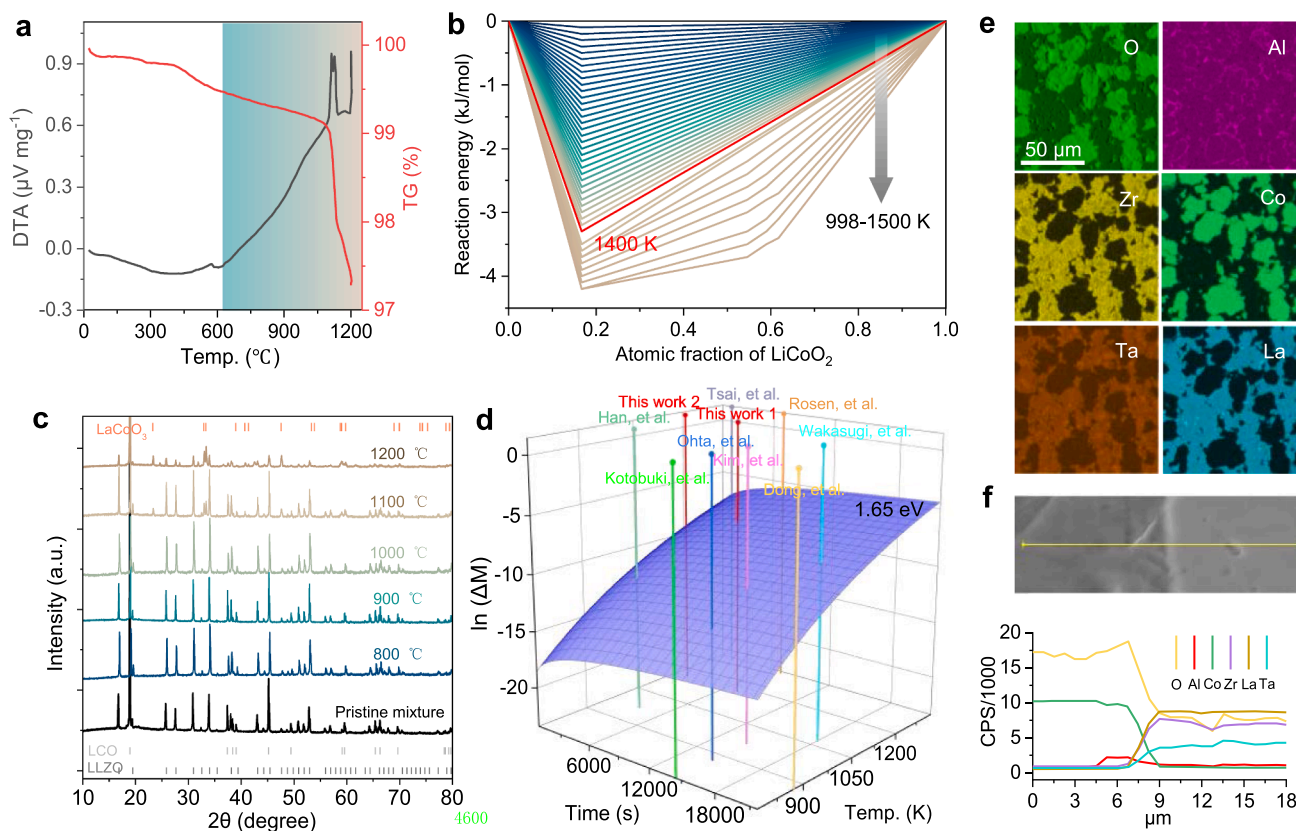

Fig. 1. (a) TG and DTA of the mixture of 50 wt.% LCO and 50 wt.% LLZO; (b) LCO/LLZO pseudo-binary phase diagram from 996 K to 1500 K with calculated data points every 10 K; (c) XRD patterns of compressed pellets of 50:50 wt.% mixture of LCO and LLZO powders after annealing over a temperature range from 800 °C to 1200 °C with a dwell time of 2 h. (d) Comparison of the interdiffusion of LCO and LLZO extracted from literature for experimental conditions selection [13,14,27, 29-34]. EDS mapping (e) and line scan (f) of SEM for co-sintered cathodes.

and cathode is relatively slow, while above this critical temperature the reaction is accelerated.

Assuming that the metastable phases are indeed products of the interdiffusion of ions, the question arises as to how interdiffusion affects the structure and performance of LLZO and LCO. To study this effect, one should be able to control the annealing parameters to choose the appropriate experimental conditions. The extent of interdiffusion should be restricted to the point where the interface is capable of being sintered, rather than waiting until the diffusion reaction reaches equilibrium, because in practical applications, interdiffusion should be avoided as much as possible. It can be assumed that the degree of interdiffusion depends on the annealing temperature as well as the dwell time according to the Arrhenius equation [28], leading to the following equation:

$$\frac{\Delta M}{t} = k = A e^{-\frac{E_a}{RT}}$$

and therefore

$$\ln(\Delta M) = \ln A - \frac{E_a}{RT} + \ln t$$

where ΔM represents the change in amount of a particular substance involved in a reaction. For example, considering the diffusion of Co-ions in LLZO, ΔM is the amount of Co-ions, t is the time interval, k is the rate constant, A is the pre-exponential factor (or frequency factor), R is the gas constant, T is the absolute temperature and E_a is the corresponding activation energy of interdiffusion. If the activation energy of interdiffusion remains constant, which should be the case for the same compounds and the same diffusing elements, it is possible to determine the degree of interdiffusion as a function of temperature and time. As an example, we have drawn an isosurface for diffusion of Co-ions to LLZO using the activation energy of 1.65 eV determined by *Mir Mehraj* Ud Din et al. [16] (Fig. 1d). Based on the intersection of the isosurface with the temperature and dwell times (such as the values reported in various publications, which are plotted as vertical lines in Fig. 1d), the extent of diffusion can be compared [13,14,27,29-34]. It is important to note that we do not perform quantitative calculations on the amount of diffusion in this study. The aim is to make comparisons based on the currently reported literature. The formula used for describing diffusion is empirical, and the dimensions of ΔM are ambiguous. Based on this comparison and the study of thermodynamics, we have chosen a temperature of 900 °C and a dwell time of 2 h as parameters at which the interdiffusion is promoted almost to its maximum value, so that the interface is well sintered but before the formation of secondary phases starts (labeled This work 1 in Fig. 1d). The selected degree of interdiffusion is higher than in the majority of publications (Fig. 1d) [13,14,27,29-34]. Scanning electron microscopy (SEM) images of compressed LLZO and LCO powders sintered under these conditions show that the powders are indeed well sintered and the interfaces are sharp and well defined. Energy dispersive X-ray spectroscopy (EDS) of the larger area (Fig. 1e) and line scans performed across the interface (Fig. 1f) show that Al has diffused extensively, especially from the edge of LCO particles to the interface, where it tends to accumulate. The diffusion of the other elements is difficult to determine accurately with EDS due to the limited resolution.

In order to investigate the structure of the compounds formed after the ion interdiffusion and its effect on the material properties, the sintering was carried out in such a way that the individual materials could be examined separately and independently of each other. For this purpose, sintered LLZO pellets were embedded in LCO powder and annealed at 900 °C for 2 h before being removed for individual examination. After treatment, the color of LLZO pellets changed from white to brown (Figure S1). Inductively coupled plasma-atomic emission spectrometry (ICP-OES) and XRD refinement showed the presence of Co-ions, which diffused into LLZO and occupied 24d positions to form

$(Li_{6.25}Al_{0.03}Co_{0.13})La_3Zr_{1.6}Ta_{0.4}O_{12}$ (LLZO:Co) (Fig. 2a) [16]. The XRD pattern of the pristine pellet is shown for comparison in Figure S2. After substitution with Co-ions, LLZO:Co still retains a cubic phase with lattice parameters of 12.94 Å, with a slight shrinkage compared to parent LLZO (12.95 Å). The Raman spectra of LLZO:Co and parent LLZO are shown in Fig. 2b. A new peak at 689.9 cm^{-1} was observed in the Raman spectra, which can be attributed to a specific vibration mode of Co-O tetrahedron [13].

A series of electrochemical measurements were performed to investigate the effects of Co-ion diffusion on the performance of the LLZO pellets (Fig. 2c-f). Electrochemical impedance spectroscopy (EIS) at room temperature showed that the total resistance, including bulk and grain boundary resistance, increased after substitution with Co-ions, corresponding to a decrease in Li-ion conductivity from 0.61 mS cm^{-1} in LLZO to 0.53 mS cm^{-1} in LLZO:Co (Fig. 2c). Impedance data were collected over a temperature range from 100 °C to −100 °C to calculate the activation energy for Li-ion diffusion. The activation energy was determined to be 0.42 eV in LLZO, while it increased to 0.44 eV in LLZO: Co (Fig. 2d). To accurately determine the electronic conductivity, DC polarization measurements were performed over 100 h. The results indicate that the electronic conductivity of both compounds is very similar. However, the decreasing trend of total conductivity is slower in LLZO:Co, possibly attributed to the higher activation energy of Li-ions in LLZO:Co. Remarkably, the final electronic conductivity of LLZO is 2.1•10^{-10} S cm^{-2}, which is an order of magnitude lower than the currently reported value of 10^{-8}–10^{-9} S cm^{-2} and almost at the same level as the conductivity of single crystal Ga-LLZO reported by Philipp et al. (Fig. 2e) [35,36]. This could be due to the fact that the electronic conductivity of LLZO depends on different dopants and defects and that measurements over 100 h have rarely been performed in the previous. Cyclic voltammetry (CV) at room temperature shows no pronounced redox properties for Co-substituted LLZO in the potential range from 3 V to 5 V and only a slightly lower onset potential of oxidation reaction (Fig. 2f). These results differ from our previous observation where clear redox peaks were observed in LLZO after sintering with LCO [17]. However, it should be mentioned that our previous experiments were performed under much harsher conditions (corresponding to stage 2 of the reaction described above), which led to the formation of secondary phases in addition to LLZO:Co. The control of interdiffusion by the choice of sintering parameters described in this work allows to selectively obtain phase-pure LLZO:Co that does not exhibit redox activity. The combination of different electrochemical methods suggests that the diffusion of Co-ions leads to a slightly reduced ionic conductivity and retained electronic conductivity of LLZO without significantly changing the redox activity.

To investigate the effect of interdiffusion on the structure and electrochemical performance of LCO, the powder was separated after annealing with LLZO pellets. According to ICP-OES analysis, the powder contains 0.25 wt.% Al, suggesting that a compound with the chemical composition $LiCo_{0.99}Al_{0.01}O_2$ is formed after heat treatment. X-ray photoelectron spectroscopy (XPS) was employed, and fine spectra were analyzed to determine the binding energy of Al, considering the possibility of its presence in Li or Co positions (Fig. 3a). In the annealed sample, the Al 2p peak appeared with a peak position at 73.0 eV. This agrees well with the reported binding energy of Al-doped LCO, suggesting that Al likely replaces Co-ions in the LCO lattice [37]. Rietveld refinement of the XRD patterns provides further information about the microstructure (Fig. 3b). For the pristine LCO, a sharp and intense (002) reflection was observed at 19.0°, indicating a highly ordered structure along the c-axis (Figure S3). In contrast, the relative intensity of the (002) reflection was significantly lower in LCO:Al, indicating a disordered structure in this direction after annealing. The possible reason for this is the diffusion of Al or Li into the transition metal layer with the occupation of the Co sites, leading to disorder in the layered structure. The lattice parameters (R -3 m hexagonal axes, $a = b = 2.82$ Å, $c = 14.06$ Å) remained unchanged after substitution. Raman spectroscopy
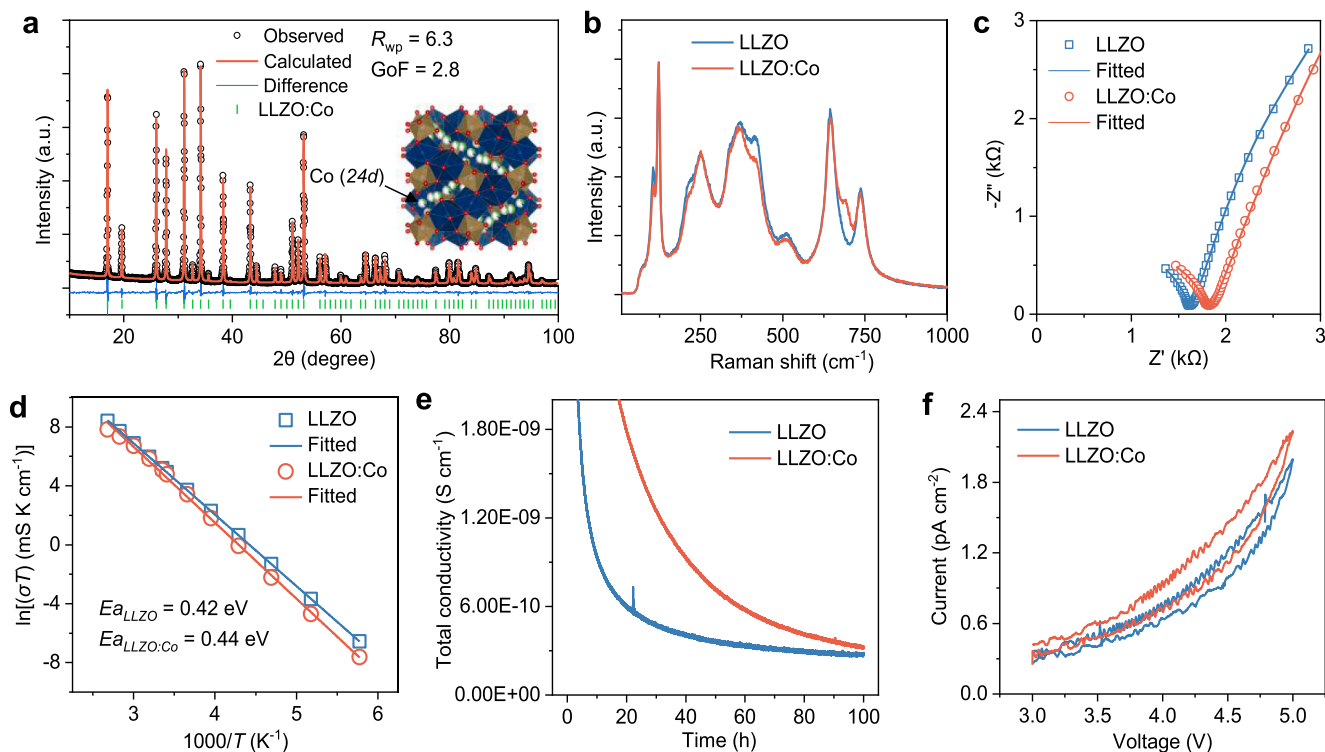
Fig. 2. (a) XRD refinement of LLZO:Co. Comparison of pristine LLZO and ion interdiffused LLZO:Co: Raman spectra (b), normalized impedance at 25 °C (c), activation energy with fit lines (d), DC polarization at 25 °C (e), and CV at 25 °C (f).
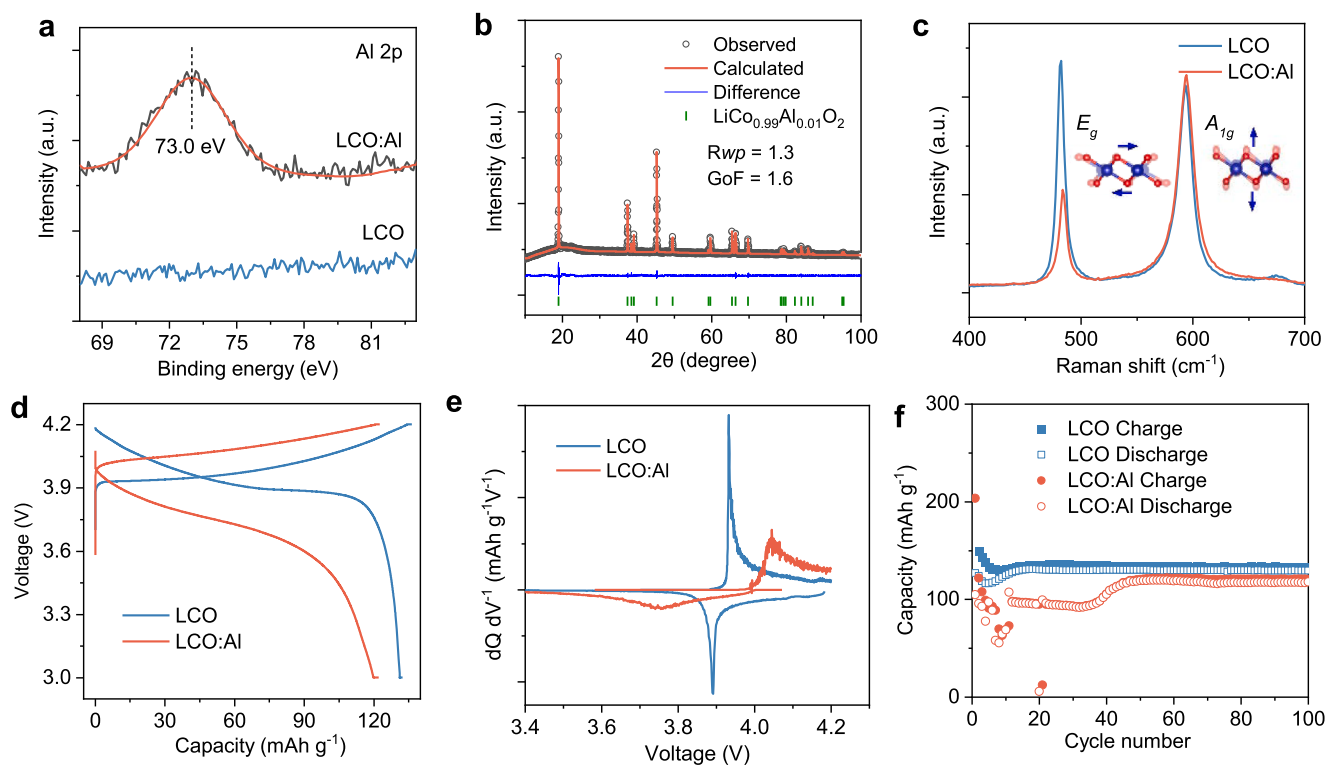

Fig. 3. (a) XPS spectra of LCO and LCO:Al. (b) XRD refinement of LCO:Al. (c) Raman spectra of LCO and LCO:Al. Galvanostatic charge/discharge curves for 50th cycle (d) and corresponding dQ/dV (e), and prolonged cycling (f) of LCO and LCO:Al at 25 °C.

provided additional insight into the structural properties of LCO:Al (Fig. 3c). The LCO exhibited two active modes, E_g (481.90 cm^{-1}) and A_{1g} (593.65 cm^{-1}), which correspond to the vibrational modes of Co-O

along the Co plane and perpendicular to the Co plane, respectively (Fig. 3c, inset) [38]. LCO:Al showed a blue shift of respective Raman lines to 483.81 cm^{-1} and 593.96 cm^{-1}, indicating the substitution of Co

positions by Al [26,39,40]. The weaker intensity observed in the E_g vibration direction for LCO:Al also suggests disorder of layer structure after interdiffusion.

The electrochemical performance of LCO and LCO:Al was further investigated with liquid electrolyte in a potential range from 3 V to 4.2 V. Galvanostatic charge/discharge cycling (Fig. 3d) and the corresponding differential curves (Fig. 3e) show distinct differences between LCO and LCO:Al. In the case of LCO, clear charge and discharge plateaus were observed at 3.93 V and 3.89 V, respectively, and the dQ/dV curves exhibited sharp peaks. The slope of the plateaus and the hysteresis between the charge and discharge curves increase for LCO:Al, and the corresponding dQ/dV curves show broadened peaks at 4.04 V and 3.75 V. These results indicate that LCO:Al exhibits a higher polarization during charging and discharging. During prolonged cycling at a low rate of 0.1 C at 25 °C (Fig. 3f), the LCO exhibits a stable capacity of ~130 mAh g^{-1}, which is typical of commercial LCO electrodes. In contrast, the capacity of LCO:Al fluctuates significantly during the first ten cycles, followed by a stable but reduced capacity of 100 mAh g^{-1} in the following twenty cycles. Thereafter, the capacity increases to 120 mAh g^{-1} and remains stable. The initial instability of capacity can be attributed to structural adjustments within the material during cycling, and the larger polarization behavior originates from the disordered layered structure. Therefore, the annealing process applied to LCO can induce structural disorder, resulting in increased polarization and a slight decrease in capacity by 7.7 %. However, this structural change does not significantly affect the cycling performance.

The results above demonstrate that heating LLZO and LCO mixtures at temperatures as low as approximately 630 °C induces interdiffusion of Al and Co atoms into LCO and LLZO lattices, respectively. This process forms metastable substituted compounds with structural and electrochemical properties that differ from those of the starting compounds. By selecting suitable sintering parameters, further undesired reactions with the formation of thermodynamically stable reaction products can be avoided. However, even with these apparently "clean" interfaces, the interdiffusion can never be completely avoided at the practical temperatures required for powder compaction, so that the products of

interdiffusion are always present at the interface. Through the above studies on the electrolyte and cathode materials, we determined that such diffusion will not result in a significant degradation of the performance of the electrolyte and cathode materials. Therefore, the reason of capacity decay may stem from battery operation.

To characterize the electrochemical performance of such interfaces and their evolution during electrochemical cycling, a half cell consisting of an LCO-LLZO composite cathode and a LLZO separator (Fig. 4a) was fabricated using field-assisted sintering technology/spark plasma sintering (FAST/SPS), as previously reported by our group [31]. According to our proposed interdiffusion model, the sintering process was conducted at a temperature of only 675 °C, which is the lowest successful temperature reported in our previous work, under a pressure of 440 MPa for 10 min in an argon atmosphere. Afterwards, the sintered cell was annealed at 900 °C for 30 min in air to crystallize the interface. The amount of diffusion is indicated in Fig. 1d as a comparison. It should be noted, that these processing conditions will reduce the interdiffusion, but will also result in a significant change in microstructure, as the reduction of the temperature from 750 to 675 °C will result in an increase of the porosity from 5 to 8% respectively [31]. However, the reduced temperatures are expected to result in less interdiffusion, resulting in lower initial performance degradation of the LLZO and LCO. This facilitates a more detailed study of the cell's performance evolution during operation. To exclude possible effects of the FAST/SPS process and subsequent annealing on the material, in particular the possible formation of secondary phases, we performed phase identification of the fabricated half cell by XRD (Figure S4). All diffraction peaks could be assigned to LLZO and LCO, indicating that no new phases were introduced by the battery fabrication process. The full cell was assembled by attaching a Li metal foil as a negative electrode to the LLZO separator. The Nyquist plot of the impedance spectra shows two characteristic semicircles and a diffusion-related slope. The equivalent circuit used to fit the impedance spectrum is shown in Figure S5. The semicircle in the high frequency range (2 MHz) is attributed to the bulk and grain boundary resistance of LLZO. The mid frequency range (3 kHz) corresponds to the interface resistance, encompassing the interface resistance
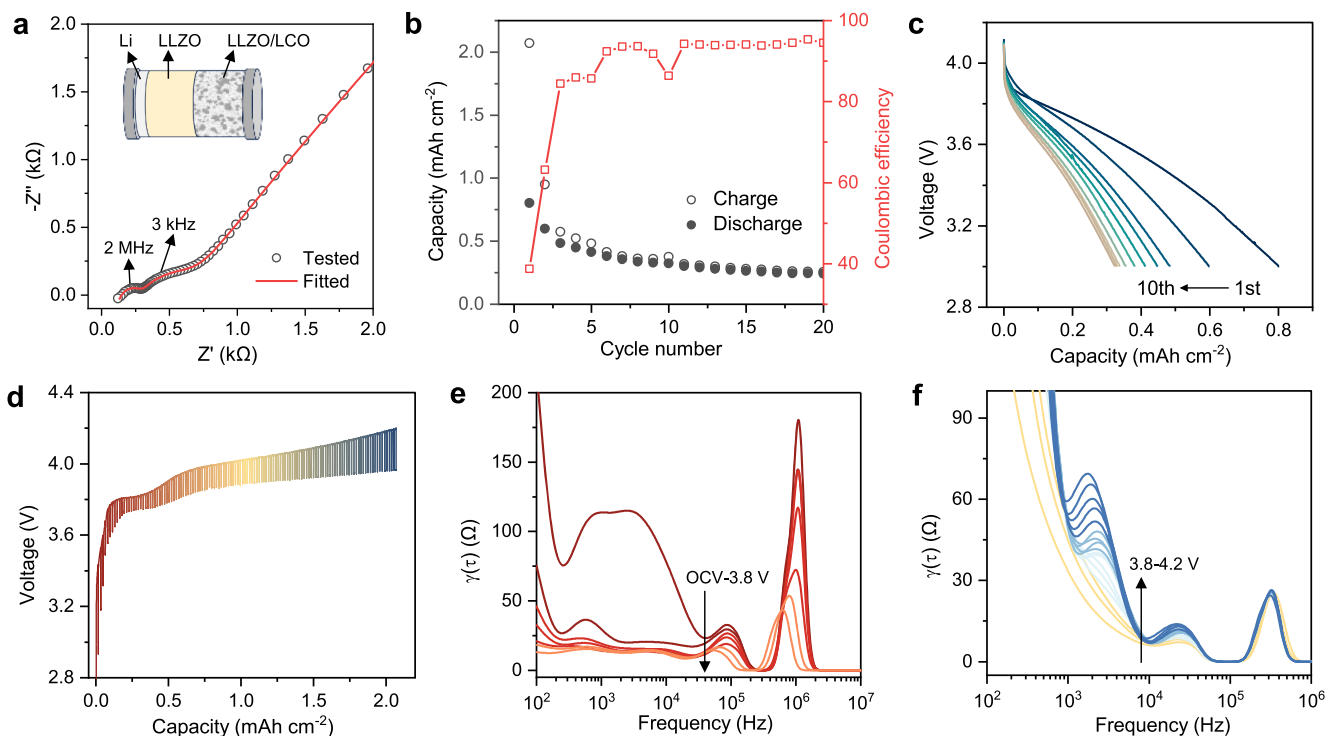

Fig. 4. Impedance of prepared cell (a) and cycle performance tested at 50 µA cm^{-2} (b) as well as corresponding discharge curves (c) measured at 60 °C. (d) Galvanostatic intermittent titration test for first charge and corresponding DRT analysis from OCV to 3.8 V (e) and 3.8 to 4.2 V (f) tested at 60 °C.

between Li and LLZO as well as LLZO and LCO. The fitted capacitance is approximately $\sim 10^{-7}$ F, which is consistent with other reported values [41].

Galvanostatic charge/discharge curves, which were recorded at 60 °C in a voltage range of 3 V to 4.2 V (Fig. 4b), show a fairly high charge capacity of 2.1 mAh cm^{-2} in the first cycle. The specific capacity is calculated to be between 70 and 95 mAh g^{-1} with 50–68 % utilization of the LCO, but due to difficulties in accurately determining the weight of the cathode, exact values cannot be provided. However, the capacity fades significantly in the following cycles, so that after the 10th cycle only 18.1 % of initial capacity is retained. The corresponding discharge curves show a considerable polarization (Fig. 4c). It is noteworthy that the coulombic efficiency in the first cycle was only 38.7 %, which calls for a closer examination of the electrochemical performance during the first charging cycle. A galvanostatic intermittent titration test (GITT) was performed during charging, with EIS characterization at the end of each intermittent step after relaxation.

As shown in Fig. 4d, as the charging potential increases, the voltage drop during the relaxation process of the battery also increases, indicating stronger polarization and higher internal resistance. The distributed relaxation times (DRT) deconvoluted from the impedance spectra are shown in Fig. 4e and f for the range from open circuit voltage (OCV) to 3.8 V and from 3.8 V to 4.2 V, respectively. The peak concentrated at a high frequency of $\sim 10^6$ Hz to 10^5 Hz is assigned to the bulk and grain boundary resistance of LLZO. This peak gradually decreases during the charging process and finally reaches a constant minimum value [42]. The second peak, which is concentrated at the intermediate frequency of $\sim 10^5$ Hz to 10^4 Hz, is associated with the anode-side interface between Li and LLZO. The height of this peak fluctuates within a small range, gradually decreasing in the OCV - 3.8 V range and slightly increasing in the 3.8 V - 4.2 V range. The intermediate frequency ranging from $\sim 10^4$ Hz to 10^3 Hz is often associated with the interface between LLZO and LCO [41]. This peak decreases significantly in the range from OCV to 3.8 V. Simultaneously the GITT experiment in Fig. 4d showed a charging plateau when reaching 3.8 V. This clearly shows that a certain process is occurring at this initial stage of cycling, which cannot be explained by Co-diffusion effects or secondary phases resulting from it. However, the process can be explained by the decomposition of another impurity, which always occurs when LLZO comes into contact with the atmosphere. When LLZO exposed to a humidity and CO$_2$-containing environment, Li$_2$CO$_3$ can form on the LLZO surface [43,44]. From literature it is known that the decomposition of this carbonate phase can be electrochemically induced under CO$_2$ outgassing, mainly occurring at the potential of 3.8 V [45]. Therefore, it is very likely that the GITT plateau at 3.8 V and a certain proportion of the peak decrease in the intermediate frequency range from $\sim 10^4$ Hz to 10^3 Hz of DRT is connected to the electrochemical Li$_2$CO$_3$ decomposition. However, the decrease prior to 3.8 V, where no carbonate decomposition is occurring, is probably related to a formation process of the interfacial structure between the LLZO and LCO [26]. Due to the previous thermal treatment, Al is already incorporated into LCO. When charging the cathode, a change in the oxidation state of Co and an associated change in charge distribution will probably cause a restructuring in the LCO. Furthermore, it is already known that LCO with a higher state of charge has a higher driving force to absorb Al, so additional Al from the LCO/LLZO interface or LLZO grains can also be incorporated into the LCO [20]. These effects would lead to a rapid restructuring of the very thin boundary layers between LCO and LLZO, which is probably visible in the DRT analysis from $\sim 10^4$ Hz to 10^3 Hz in the interface impedance decrease at the start of the charging step. Since the interfaces are very thin in the nanometer to micrometer range, the processes are rather quick and the change in impedance is only observable in the first potential step, while in the bulk region $\sim 10^6$ Hz to 10^5 Hz more materials are affected and smaller changes are observable over more potential steps.

The deterioration in performance could be due to either cathode-side or anode-side degradation. The possibility of degradation on the anode side was initially ruled out. The LLZO electrolyte pellets were prepared using the same procedure as the half cells and then assembled into symmetrical Li cells for critical current density (CCD) and cycling tests (Figure S6). The results showed that the electrolyte can withstand a maximum current density of 450 µA cm^{-2} and cycle for more than 280 h at a current density of 50 µA cm^{-2}, which was also used for the cycling of the full cells. The capacity degradation of the separators is much lower than that of the full cells after the same number of cycles, indicating that the drop in capacity in the full cell is not due to degradation on the anode side. Therefore, the capacity degradation should be attributed to the degradation of the cathode. To understand the possible reasons for the cathode degradation and the evolution of the interfacial structure, the battery was disassembled after cycling and the composite cathode was characterized by nuclear magnetic resonance (NMR) and SEM to obtain information on the evolution of chemical surrounding and the microstructure. The solid-state ^{27}Al NMR spectra of the sintered, additionally annealed and cycled electrode as well as the original LLZO and LCO powders are presented in Fig. 5a. The signals concentrated at 80.8 ppm and 62.4 ppm are attributed to Al-O tetrahedral coordination, primarily originating from Al at the 24d position of LLZO [46]. The chemical shift at 13.6 ppm is commonly assigned to Al-O hexahedral coordination [47]. In the original powder, this peak exhibits a very weak intensity, suggesting the possible presence of a small amount of secondary phase in LLZO, such as LaAlO$_3$. In the electrode sintered via FAST/SPS and the annealed electrode, this peak persists but is not intensified. This suggests that the diffusion of Al-ions during the electrode preparation process is weak, and only a small amount of Al-ions diffuse into the LCO because of Al having hexahedral coordination in both Li and Co positions within LCO. In the cycled electrode, this peak intensifies and tends to split into two peaks, indicating two different chemical environments of [AlO$_6$]. In addition, a series of weaker signals at 54.5 ppm, 76.0 ppm, and 91.1 ppm can be seen in the cycled electrode. These positions are often associated with Al tetrahedral coordination compounds [47,48]. These observations can be attributed to the diffusion of Al from the LLZO into the LCO, or the formation of secondary phases during the electrochemical cycling. Throughout the charge/discharge process, the external electric field or local potential imbalance may prompt the diffusion of the Al. Following the de-lithiation of LCO, the Co-ions change to a higher oxidation state, potentially leading to side reactions with the LLZO [20]. The structure evolution induced by the electrochemical process may exert a more detrimental effect on the performance of the electrolyte and cathode. Specifically, the formation of new phases may impede Li-ions transport and elevate the internal resistance of the battery.

Fig. 5b shows a backscatter-electron image of the as-prepared cathode. The dark contrast material is LCO, and the light contrast material is LLZO. The typical SEM image of the cathode prior to cycling shows a well sintered and connected interface between LLZO and LCO particles. The rather large porosity compared to samples prepared in our previous work is apparent, especially the micro-porosity in between the smaller LLZO grains can be attributed to the lower sintering temperature, whereas at 750 °C the LLZO showed a much denser microstructure with macropores [20,26]. The SEM image of the cycled electrode is shown in Fig. 5c. In contrast to our previous work, after five charge/discharge cycles cracks can already be observed at the LCO/LLZO interface. Since both LLZO and LCO are hard compounds with a Young's modulus of more than 100 GPa and LCO has a volume change around 5 % during lithiation/de-lithiation, enormous stresses can occur, destroying the sintered interface. Due to the lower strength in the interface area compared to the bulk phase, the stresses generated during repeated lithiation/de-lithiation processes cause damage to the interface region [49]. This leads to the formation of cracks and a subsequent increase in resistance, which hinders the efficient transport of ions and electrons, resulting in the observed capacity decay and impedance increase. From this observation it now becomes obvious, that a balance must be reached for optimizing the processing conditions with respect to cation
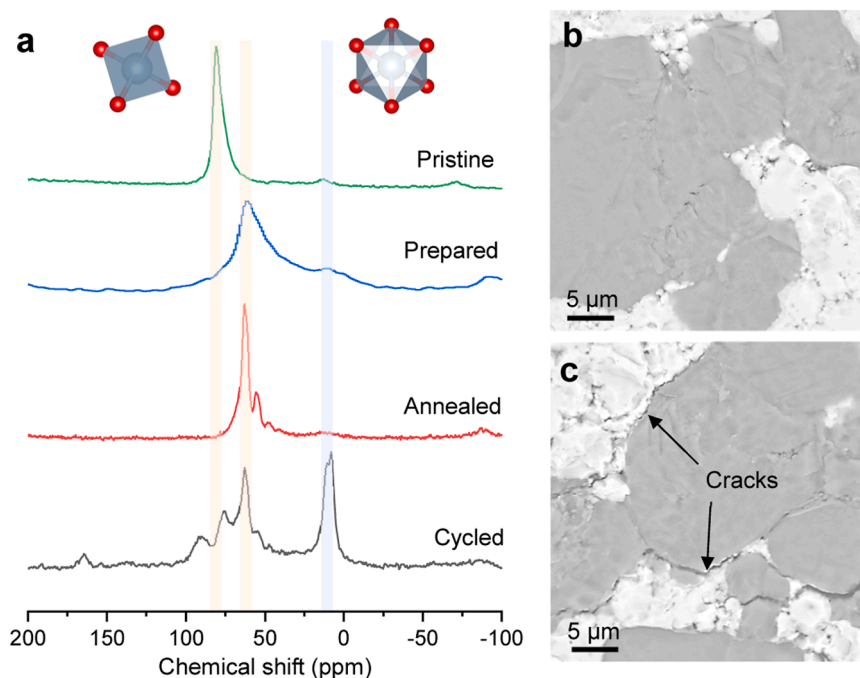
Fig. 5. Al^{27} NMR measurements of the mixture of LCO and LLZO (green), FAST/SPS prepared (blue), additionally annealed (red) and cycled electrodes (black). SEM images of FAST/SPS prepared/additionally annealed electrode before cycling (b) and after 5 cycles (c).

interdiffusion and mechanical integrity.

3. Conclusion

All-solid-state batteries featuring a fully ceramic electrode composed of LLZO and LCO were investigated regarding the degradation effects during processing and electrochemical cycling. Below a critical temperature of 1100 °C, reaction products are thermodynamically stable but kinetically hindered, and rather long sintering times can be realized. However, at such high temperatures, strong cation interdiffusion of mainly Al and Co-ions takes place and can be observed even down to 630 °C, altering both LLZO and LCO especially at the interfaces. Nevertheless, these results provide a processing window, in which a reaction between LLZO and LCO can be avoided and the cation interdiffusion can be minimized by careful choice of the heat treatment parameters.

To investigate the effect of cation interdiffusion in the bulk materials, we derived a formula for interdiffusion between LLZO and LCO. We then selected sintering parameters of 900 °C for 2 h where secondary phase formation is suppressed, but interdiffusion promoted. Subsequent studies of LLZO showed that the diffusion of 0.13 Co per formula unit (*pfu*), occupying the 24d position, did not have a significant impact on its ionic conductivity, electronic insulation or electrochemical stability. In contrast for LCO, the substitution of 0.01 *pfu* Al and the induced disorder in the layered structure can increase the polarization during lithiation/de-lithiation. However, the cycling stability of the electrode remained unaffected in subsequent electrochemical testing. A full inorganic cell based on LLZO, LCO and Li metal was constructed using FAST/SPS with parameters that would even lower the interdiffusion between LCO and LLZO. The cell showed good initial performance but similar degradation during cycling. The investigation into the evolution of Al coordination chemistry and interfacial structure revealed the impact of the Al diffusion on the cycling degradation. In contrast to our earlier works, the change in processing parameters resulted in a more porous microstructure, leading to the development of cracks along the LCO/LLZO interface during cycling and thus the observed cycling degradation.

These results again emphasize the necessity to balance between

mechanical properties and chemical reactions during high temperature fabrication of ceramic-based all-solid-state batteries. The model derived here can be used to estimate cation interdiffusion and, together with microstructural analysis, allows quick optimization of the processing parameters. However, the underlying electrochemical driven cation interdiffusion and related cycling degradation needs to be addressed on a more fundamental level, e.g. via core-shell structures or coatings. In conclusion, process and materials optimization based on mechanistic understanding can enable fully inorganic, oxide-ceramic based batteries with high safety and high performance for future energy applications.

4. Experimental Section

4.1. Synthesis and fabrication of Li$_{6.45}$La$_3$Zr$_{1.6}$Al$_{0.05}$Ta$_{0.4}$O$_{12}$ powder, pellets and composite cathode

The starting materials used in the study included LiOH•H$_2$O (99 %, AppliChem GmbH, Darmstadt, Germany), La$_2$O$_3$ (99.9 %, Merck KGaA, Darmstadt, Germany, pre-dried at 900 °C for 10 h), ZrO$_2$ (99.5 %, Alfa Aesar GmbH & Co KG, Karlsruhe, Germany), Ta$_2$O$_5$ (Inframat, 99.95 %), and Al$_2$O$_3$ (99.9 %, Inframat Advanced Materials LLC, Manchester, CT, USA). These materials were weighed in stoichiometric proportions in 100 g batches and then ground using an electrical mortar grinder (RM 200, Retsch GmbH, Haan, Germany) for 1 hour. The homogenized powder was then used to prepare pellets, which were pressed using a uniaxial press with a diameter of 45 mm and a pressure of 20 MPa. The pellets were calcined twice in Al$_2$O$_3$ crucibles. The first calcination step was carried out at 850 °C, followed by a second calcination step at 1000 °C for 20 h each. After each calcination step, the pellets were ground into powder form and repressed again. For pellet preparation, uniaxial pellets with a diameter of 13 mm and compressed at 113 MPa were sintered in an Al$_2$O$_3$ crucible, placed on a MgO plate, along with an LLZO powder sheet at 1175 °C, with a dwell time of 10 h. The sample used for the study of cation interdiffusion study by SEM and DES analysis was prepared by compressing equal quantities of LCO (MTI, battery grade) and LLZO powder at 400 MPa and then sintering at 900 °C for 2 h. To investigate the effects of cation interdiffusion on the individual

performance of the LLZO and LCO phases, the LLZO pellet, which was pre-sintered at 1175 °C for 10 h, was embedded in an equal weight amount of LCO powder. The LCO powder was manually pressed on both sides of the LLZO pellet and then transferred to a crucible and annealed at 900 °C for two hours. After annealing, the LCO was mechanically scraped from the surface of LLZO and collected to prepare an electrode for electrochemical characterization. The LLZO pellet was manually polished from both sides to remove the residual LCO and used for electrochemical characterization. The field-assisted sintering technology method was carried out following our previous work to prepare cathode composite [31]. For the preparation of half cells, first pour a powder mixture of 0.5 g LCO and LLZO (1:1 wt ratio) into a mold and press at 50 MPa, then add 1 g LLZO powder and press again at the same pressure. Sintering takes place at a temperature of 675 °C and has a dwell time of 10 min at Ar flow in the HPD5 FAST/SPS device (FCT Systeme). The heating rate is $100\,°C\,min^{-1}$, and the cooling rate is $20\,°C\,min^{-1}$. After sintering, the half cells were annealed at 900 °C for 30 min. The preparation of the electrolyte pellets followed the same procedure as for the half cell preparation, but without LCO added. The cathode side and the separator side of prepared half cell were polished to achieve a thickness of 80–100 μm and 0.8–1 mm for the cathode layer and the separator layer, respectively.

4.2. Material characterization

Thermogravimetric and differential thermal analysis were performed using the Netzsch STA449C Jupiter thermoanalyzer with a heating rate of $5\,°C\,min^{-1}$ in the temperature range from room temperature to 1600 °C. The chemical composition was analyzed using inductively coupled plasma-optical emission spectrometry with a Thermo Scientific iCAP7600 instrument (Thermo Fischer Scientific, Waltham, MA, USA). X-ray diffraction was conducted using a D4 ENDEAVOR instrument (Bruker Corporation, Billerica, MA, USA) with Cu Kα radiation. Rietveld refinement was applied within a 2θ range of 10–140° for crystal structural refinement and determination of lattice parameters using the GSAS II package. Scanning electron microscope images were obtained using a Zeiss EVO 15 instrument (Carl Zeiss Microscopy Deutschland GmbH, Oberkochen, Germany) coupled with an energy-dispersive X-ray spectroscopy detector X-max 80 (Oxford Instruments plc, Abingdon, UK). Raman spectroscopy was performed with a Renishaw invia Qontor Raman Microscope equipped with a solid-state 532 nm excitation laser and a $2400\,l\,mm^{-1}$ grating.

Solid state magic angle spinning (MAS) NMR measurements were performed on a Bruker Ascend 500 magnet (11.7 T) equipped with a NEO console operating at a ^{27}Al resonance frequency of 130.32 MHz, using a Bruker 3.2 mm three channel MAS probe head. The MAS rate was set to 20 kHz for all measurements. Single pulse and Hahn echo one-dimensional (1D) measurements were recorded with pulse lengths between 1 and 3 μs. A recycle delay of between 0.2 and 1 s was used and up to 30,720 scans each were acquired.

4.3. Electrochemical characterization

The electrodes of LCO and LCO:Al were prepared by mixing 80 wt% active materials, 10 wt% carbon black (Aladdin), and 10 wt% polyvinylidene fluoride binder (Aladdin) dissolved in N-methyl-2-pyrrolidinone (Aladdin 99.5 %) to make slurry. The slurry was coated on Al foils and dried at 80 °C under vacuum overnight to remove the solvent, and then pressed and punched into a disk. The batteries were assembled in CR2032-type cell in an argon filled glove box, the Li metal disk (Aladdin, 99 %) was used as counter electrode, and glass microfiber (Whatman) was used as the separator. The electrolyte was 1 M lithium hexafluorophosphate dissolved in ethylene carbonate and diethyl carbonate (1/1 by volume). All-solid-state batteries were also assembled in a glove box. Li metal disk was attached to the prepared half cell and heated at 300 °C for 5 min before being assembled into the Swagelok battery for testing.

All electrochemical measurements were performed using a BioLogic VMP-300 Multichannel Potentiostat. Electrochemical impedance spectroscopy was conducted over a frequency range of 7 MHz to 1 Hz, applying a perturbation field with an amplitude of 10 mV at a temperature of 25 °C. The obtained impedance spectra were fitted using the ZView software. DC polarization experiments were carried out by applying a constant voltage of 0.2 V for a duration of 100 h at a temperature of 25 °C. Cyclic voltammetry measurements were recorded with a scan rate of $0.1\,mV\,s^{-1}$ within a voltage window of 3 V to 5 V, also at 25 °C. Galvanostatic charge/discharge tests of $LiCoO_2$ and $LiCo_{0.99}Al_{0.01}O_2$ were performed using a current density of 0.1 C at a temperature of 25 °C. Similarly, the galvanostatic charge/discharge test of the prepared solid-state cathode was conducted at a current density of $50\,\mu A\,cm^{-2}$ and a temperature of 60 °C. To determine the activation energy, electrochemical impedance spectra were recorded using a Novocontrol Technologies Alpha-A impedance spectrometer. The measurements were carried out over a frequency range of 10 MHz to 1 Hz with a field perturbation of 20 mV. The temperature-dependent impedance measurements were recorded in a temperature-controlled chamber within the temperature range of −100 °C to 100 °C.

4.4. Computation

The formation energies obtained from Materials Project with r2SCAN metaGGA functional, and the Gibbs energies were calculated based on the methods developed by C. J. Bartel et al. for pseudo-binary phase diagram calculation [50].

CRediT authorship contribution statement

Kai Yao: Writing – original draft, Visualization, Software, Methodology, Investigation, Formal analysis, Data curation, Conceptualization. **Walter Sebastian Scheld:** Writing – review & editing, Formal analysis, Data curation. **Qianli Ma:** Investigation. **Yuan Zeng:** Conceptualization. **Swapna Ganapathy:** Investigation. **Martin Ihrig:** Investigation. **Ruijie Ye:** Writing – review & editing. **Meng Ma:** Writing – review & editing. **Vivien Kiyek:** Writing – review & editing. **Olivier Guillon:** Writing – review & editing. **Mark Huijben:** Writing – review & editing, Supervision, Funding acquisition. **Johan E. ten Elshof:** Writing – review & editing, Supervision, Funding acquisition. **Martin Finsterbusch:** Writing – review & editing, Writing – original draft, Resources, Conceptualization. **Dina Fattakhova-Rohlfing:** Writing – review & editing, Writing – original draft, Supervision, Resources, Project administration, Methodology, Funding acquisition, Conceptualization.

Supplementary materials

Supplementary material associated with this article can be found, in the online version, at doi:10.1016/j.ensm.2024.103662.

References

[1] J. Janek, W.G. Zeier, Challenges in speeding up solid-state battery development, Nat. Energy 8 (2023) 230–240, https://doi.org/10.1038/s41560-023-01208-9.

[2] R. Chen, Q. Li, X. Yu, L. Chen, H. Li, Approaching practically accessible solid-state batteries: stability issues related to solid electrolytes and interfaces, Chem. Rev. 120 (2020) 6820–6877, https://doi.org/10.1021/acs.chemrev.9b00268.

[3] L. Zhang, Q. Zhuang, R. Zheng, Z. Wang, H. Sun, H. Arandiyan, Y. Wang, Y. Liu, Z. Shao, Recent advances of Li$_7$La$_3$Zr$_2$O$_{12}$-based solid-state lithium batteries towards high energy density, Energy Storage Mater 49 (2022) 299–338, https://doi.org/10.1016/j.ensm.2022.04.026.

[4] C. Wang, K. Fu, S.P. Kammampata, D.W. McOwen, A.J. Samson, L. Zhang, G. T. Hitz, A.M. Nolan, E.D. Wachsman, Y. Mo, et al., Garnet-type solid-state electrolytes: materials, interfaces, and batteries, Chem. Rev. 120 (2020) 4257–4300, https://doi.org/10.1021/acs.chemrev.9b00427.

[5] T. Thompson, S. Yu, L. Williams, R.D. Schmidt, R. Garcia-Mendez, J. Wolfenstine, J.L. Allen, E. Kioupakis, D.J. Siegel, J. Sakamoto, Electrochemical window of the Li-Ion solid electrolyte Li$_7$La$_3$Zr$_2$O$_{12}$, ACS Energy Lett 2 (2017) 462–468, https://doi.org/10.1021/acsenergylett.6b00593.

[6] G.V. Alexander, C. Shi, J. O'Neill, E.D. Wachsman, Extreme lithium-metal cycling enabled by a mixed ion- and electron-conducting garnet three-dimensional architecture, Nat. Mater. 22 (2023) 1136–1143, https://doi.org/10.1038/s41563-023-01627-9.

[7] Y. Ren, T. Danner, A. Moy, M. Finsterbusch, T. Hamann, J. Dippell, T. Fuchs, M. Müller, R. Hoft, A. Weber, et al., Oxide-based solid-state batteries: a perspective on composite cathode architecture, Adv. Energy Mater. 13 (2022) 2201939, https://doi.org/10.1002/aenm.202201939.

[8] S. Yu, R.D. Schmidt, R. Garcia-Mendez, E. Herbert, N.J. Dudney, J.B. Wolfenstine, J. Sakamoto, D.J. Siegel, Elastic properties of the solid electrolyte Li$_7$La$_3$Zr$_2$O$_{12}$ (LLZO), Chem. Mater. 28 (2016) 197–206, https://doi.org/10.1021/acs.chemmater.5b03854.

[9] W.Z. Huang, C.Z. Zhao, P. Wu, H. Yuan, W.E. Feng, Z.Y. Liu, Y. Lu, S. Sun, Z.H. Fu, J.K. Hu, et al., Anode-free solid-state lithium batteries: a review, Adv. Energy Mater. 12 (2022) 2201044, https://doi.org/10.1002/aenm.202201044.

[10] M. Qu, W.H. Woodford, J.M. Maloney, W.C. Carter, Y.-M. Chiang, K.J. Van Vliet, Nanomechanical quantification of elastic, plastic, and fracture properties of LiCoO$_2$, Adv. Energy Mater. 2 (2012) 940–944, https://doi.org/10.1002/aenm.201200107.

[11] L.J. Miara, W.D. Richards, Y.E. Wang, G. Ceder, First-principles studies on cation dopants and electrolyte|cathode interphases for lithium garnets, Chem. Mater. 27 (2015) 4040–4047, https://doi.org/10.1021/acs.chemmater.5b01023.

[12] L. Miara, A. Windmuller, C.L. Tsai, W.D. Richards, Q. Ma, S. Uhlenbruck, O. Guillon, G. Ceder, About the compatibility between high voltage spinel cathode materials and solid oxide electrolytes as a function of temperature, ACS Appl. Mater. Interfaces 8 (2016) 26842–26850, https://doi.org/10.1021/acsami.6b09059.

[13] C.-L. Tsai, Q. Ma, C. Dellen, S. Lobe, F. Vondahlen, A. Windmüller, D. Grüner, H. Zheng, S. Uhlenbruck, M. Finsterbusch, et al., A garnet structure-based all-solid-state Li battery without interface modification: resolving incompatibility issues on positive electrodes, Sustain. Energy Fuels 3 (2019) 280–291, https://doi.org/10.1039/c8se00436f.

[14] M. Rosen, M. Finsterbusch, O. Guillon, D. Fattakhova-Rohlfing, Free standing dual phase cathode tapes-scalable fabrication and microstructure optimization of garnet-based ceramic cathodes, J. Mater. Chem. A 10 (2022) 2320–2326, https://doi.org/10.1039/d1ta07194g.

[15] A.M. Nolan, E.D. Wachsman, Y. Mo, Computation-guided discovery of coating materials to stabilize the interface between lithium garnet solid electrolyte and high-energy cathodes for all-solid-state lithium batteries, Energy Storage Mater. 41 (2021) 571–580, https://doi.org/10.1016/j.ensm.2021.06.027.

[16] W.S. Scheld, K. Kim, C. Schwab, A.C. Moy, S.K. Jiang, M. Mann, C. Dellen, Y. J. Sohn, S. Lobe, M. Ihrig, et al., The riddle of dark LLZO: cobalt diffusion in garnet separators of solid-state lithium batteries, Adv. Funct. Mater. 33 (2023) 2302939, https://doi.org/10.1002/adfm.202302939.

[17] M.M.U. Din, L. Ladenstein, J. Ring, D. Knez, S. Smetaczek, M. Kubicek, M. Sadeqi-Moqadam, S. Ganschow, E. Salagre, E.G. Michel, et al., A guideline to mitigate interfacial degradation processes in solid-state batteries caused by cross diffusion, Adv. Funct. Mater. 33 (2023) 2303680, https://doi.org/10.1002/adfm.202303680.

[18] A.Y. Hou, C.Y. Huang, C.L. Tsai, C.W. Huang, R. Schierholz, H.Y. Lo, H. Tempel, H. Kungl, R.A. Eichel, J.K. Chang, et al., All-solid-state garnet-based lithium batteries at work-in operando TEM investigations of delithiation/lithiation process and capacity degradation mechanism, Adv. Sci. 10 (2023) e2205012, https://doi.org/10.1002/advs.202205012.

[19] Y. Xiao, Y. Wang, S.-H. Bo, J.C. Kim, L.J. Miara, G. Ceder, Understanding interface stability in solid-state batteries, Nat. Rev. Mater. 5 (2019) 105–126, https://doi.org/10.1038/s41578-019-0157-5.

[20] M. Ihrig, M. Finsterbusch, A.M. Laptev, C.H. Tu, N.T.T. Tran, C.A. Lin, L.Y. Kuo, R. Ye, Y.J. Sohn, P. Kaghazchi, et al., Study of LiCoO$_2$/Li$_7$La$_3$Zr$_2$O$_{12}$:Ta interface degradation in all-solid-state lithium batteries, ACS Appl. Mater. Interfaces 14 (2022) 11288–11299, https://doi.org/10.1021/acsami.1c22246.

[21] M. Finsterbusch, T. Danner, C.L. Tsai, S. Uhlenbruck, A. Latz, O. Guillon, High capacity garnet-based all-solid-state lithium batteries: fabrication and 3D-microstructure resolved modeling, ACS Appl. Mater. Interfaces 10 (2018) 22329–22339, https://doi.org/10.1021/acsami.8b06705.

[22] Y. Zhu, X. He, Y. Mo, Origin of outstanding stability in the lithium solid electrolyte materials: insights from thermodynamic analyses based on first-principles calculations, ACS Appl. Mater. Interfaces 7 (2015) 23685–23693, https://doi.org/10.1021/acsami.5b07517.

[23] J. Neises, W.S. Scheld, A.-R. Seok, S. Lobe, M. Finsterbusch, S. Uhlenbruck, R. Schmechel, N. Benson, Study of thermal material properties for Ta- and Al-substituted Li$_7$La$_3$Zr$_2$O$_{12}$ (LLZO) solid-state electrolyte in dependency of temperature and grain size, J. Mater. Chem. A 10 (2022) 12177–12186, https://doi.org/10.1039/d2ta00323f.

[24] C.J. Bartel, S.L. Millican, A.M. Deml, J.R. Rumptz, W. Tumas, A.W. Weimer, S. Lany, V. Stevanovic, C.B. Musgrave, A.M. Holder, Physical descriptor for the Gibbs energy of inorganic crystalline solids and temperature-dependent materials chemistry, Nat. Commun. 9 (2018) 4168, https://doi.org/10.1038/s41467-018-06682-4.

[25] K. Park, B.-C. Yu, J.-W. Jung, Y. Li, W. Zhou, H. Gao, S. Son, J.B. Goodenough, Electrochemical nature of the cathode interface for a solid-state lithium-ion battery: interface between LiCoO$_2$ and Garnet-Li$_7$La$_3$Zr$_2$O$_{12}$, Chem. Mater. 28 (2016) 8051–8059, https://doi.org/10.1021/acs.chemmater.6b03870.

[26] M. Ihrig, L.Y. Kuo, S. Lobe, A.M. Laptev, C.A. Lin, C.H. Tu, R. Ye, P. Kaghazchi, L. Cressa, S. Eswara, et al., Thermal recovery of the electrochemically degraded LiCoO$_2$/Li$_7$La$_3$Zr$_2$O$_{12}$:Al,Ta Interface in an all-solid-state lithium battery, ACS Appl. Mater. Interfaces 15 (2023) 4101–4112, https://doi.org/10.1021/acsami.2c20004.

[27] Y. Kim, D. Kim, R. Bliem, G. Vardar, I. Waluyo, A. Hunt, J.T. Wright, J.P. Katsoudas, B. Yildiz, Thermally driven interfacial degradation between Li7La3Zr2O12 electrolyte and LiNi0.6Mn0.2Co0.2O2 cathode, Chem. Mater. 32 (2020) 9531–9541. doi:10.1021/acs.chemmater.0c02261.

[28] M. Menzinger, R. Wolfgang, The meaning and use of the Arrhenius activation energy, Angew. Chem. Int. Edit. 8 (1969) 438–444, https://doi.org/10.1002/anie.196904381.

[29] Y. Dong, P. Su, G. He, H. Zhao, Y. Bai, Constructing compatible interface between Li$_7$La$_3$Zr$_2$O$_{12}$ solid electrolyte and LiCoO$_2$ cathode for stable cycling performances at 4.5 V, Nanoscale 13 (2021) 7822–7830, https://doi.org/10.1039/d1nr01079d.

[30] S. Ohta, T. Kobayashi, J. Seki, T. Asaoka, Electrochemical performance of an all-solid-state lithium ion battery with garnet-type oxide electrolyte, J. Power Sources 202 (2012) 332–335, https://doi.org/10.1016/j.jpowsour.2011.10.064.

[31] M. Ihrig, M. Finsterbusch, C.-L. Tsai, A.M. Laptev, C.-h. Tu, M. Bram, Y.J. Sohn, R. Ye, S. Sevinc, S.-k. Lin, et al., Low temperature sintering of fully inorganic all-solid-state batteries-Impact of interfaces on full cell performance, J. Power Sources 482 (2021) 228905, https://doi.org/10.1016/j.jpowsour.2020.228905.

[32] F. Han, J. Yue, C. Chen, N. Zhao, X. Fan, Z. Ma, T. Gao, F. Wang, X. Guo, C. Wang, Interphase engineering enabled all-ceramic lithium battery, Joule 2 (2018) 497–508, https://doi.org/10.1016/j.joule.2018.02.007.

[33] J. Wakasugi, H. Munakata, K. Kanamura, Thermal stability of various cathode materials against Li$_{6.25}$Al$_{0.25}$La$_3$Zr$_2$O$_{12}$ electrolyte, Electrochemistry 85 (2017) 77–81, https://doi.org/10.5796/electrochemistry.85.77.

[34] M. Kotobuki, K. Kanamura, Y. Sato, T. Yoshida, Fabrication of all-solid-state lithium battery with lithium metal anode using Al$_2$O$_3$-added Li$_7$La$_3$Zr$_2$O$_{12}$ solid electrolyte, J. Power Sources 196 (2011) 7750–7754, https://doi.org/10.1016/j.jpowsour.2011.04.047.

[35] X. Liu, R. Garcia-Mendez, A.R. Lupini, Y. Cheng, Z.D. Hood, F. Han, A. Sharafi, J. C. Idrobo, N.J. Dudney, C. Wang, et al., Local electronic structure variation resulting in Li 'filament' formation within solid electrolytes, Nat. Mater. 20 (2021) 1485–1490, https://doi.org/10.1038/s41563-021-01019-x.

[36] M. Philipp, B. Gadermaier, P. Posch, I. Hanzu, S. Ganschow, M. Meven, D. Rettenwander, G.J. Redhammer, H.M.R. Wilkening, The electronic conductivity of single crystalline Ga-stabilized cubic Li$_7$La$_3$Zr$_2$O$_{12}$: a technologically relevant parameter for all-solid-state batteries, Adv. Mater. Interfaces 7 (2020) 2000450, https://doi.org/10.1002/admi.202000450.

[37] B. Xiao, Q. Tang, X. Dai, F. Wu, H. Chen, J. Li, Y. Mai, Y. Gu, Enhanced interfacial kinetics and high rate performance of LiCoO$_2$ thin-film electrodes by Al doping and in situ Al$_2$O$_3$ coating, ACS Omega 7 (2022) 31597–31606, https://doi.org/10.1021/acsomega.2c04665.

[38] M. Inaba, Y. Iriyama, Z. Ogumi, Y. Todzuka, A. Tasaka, Raman study of layered rock-salt LiCoO$_2$ and its electrochemical lithium deintercalation, J. Raman Spectrosc. 28 (1997) 613–617, https://doi.org/10.1002/(SICI)1097-4555(199708)28:8<613::AID-JRS138>3.0.CO;2-T.

[39] T. Gross, C. Hess, Raman diagnostics of LiCoO$_2$ electrodes for lithium-ion batteries, J. Power Sources 256 (2014) 220–225, https://doi.org/10.1016/j.jpowsour.2014.01.084.

[40] N. Amdouni, H. Zarrouk, F. Soulette, C. Julien, LiAl$_y$Co$_{1-y}$O$_2$ (0.0≤y≤0.3) intercalation compounds synthesized from the citrate precursors, Mater. Chem. Phys. 80 (2003) 205–214, https://doi.org/10.1016/S0254-0584(02)00491-1.

[41] G. Vardar, W.J. Bowman, Q. Lu, J. Wang, R.J. Chater, A. Aguadero, R. Seibert, J. Terry, A. Hunt, I. Waluyo, et al., Structure, chemistry, and charge transfer resistance of the interface between Li$_7$La$_3$Zr$_2$O$_{12}$ electrolyte and LiCoO$_2$ cathode, Chem. Mater 30 (2018) 6259–6276, https://doi.org/10.1021/acs.chemmater.8b01713.

[42] I.N. David, T. Thompson, J. Wolfenstine, J.L. Allen, J. Sakamoto, B. Viyas, Microstructure and Li-Ion conductivity of hot-pressed cubic $Li_7La_3Zr_2O_{12}$, J. Am. Ceram. Soc. 98 (2015) 1209–1214, https://doi.org/10.1111/jace.13455.

[43] D. Peltzer, J. Múnera, L. Cornaglia, Operando Raman spectroscopic studies of lithium zirconates during CO_2 capture at high temperature, RSC Adv. 6 (2016) 8222–8231, https://doi.org/10.1039/C5RA21970A.

[44] R. Ye, M. Ihrig, N. Imanishi, M. Finsterbusch, E. Figgemeier, A review on Li^+/H^+ exchange in garnet solid electrolytes: from instability against humidity to sustainable processing in water, ChemSusChem 14 (2021) 4397–4407, https://doi.org/10.1002/cssc.202101978.

[45] A.A. Delluva, J. Kulberg-Savercool, A. Holewinski, Decomposition of trace Li_2CO_3 during charging leads to cathode interface degradation with the solid electrolyte LLZO, Adv. Funct. Mater. 31 (2021) 2103716, https://doi.org/10.1002/adfm.202103716.

[46] B. Karasulu, S.P. Emge, M.F. Groh, C.P. Grey, A.J. Morris, Al/Ga-Doped $Li_7La_3Zr_2O_{12}$ garnets as Li-Ion solid-state battery electrolytes: atomistic insights into local coordination environments and their influence on ^{17}O, ^{27}Al, and ^{71}Ga NMR spectra, J. Am. Chem. Soc. 142 (2020) 3132–3148, https://doi.org/10.1021/jacs.9b12685.

[47] M. Haouas, F. Taulelle, C. Martineau, Recent advances in application of ^{27}Al NMR spectroscopy to materials science, Prog. Nucl. Magn. Reson. Spectrosc. 94-95 (2016) 11–36, https://doi.org/10.1016/j.pnmrs.2016.01.003.

[48] X. Zhang, H. Huo, Nuclear magnetic resonance studies of organic-inorganic composite solid electrolytes, Magn. Resonan. Lett. 1 (2021) 142–152, https://doi.org/10.1016/j.mrl.2021.10.004.

[49] R. Mücke, N. Yaqoob, M. Finsterbusch, F. Al-Jaljouli, P. Kaghazchi, D. Fattakhova-Rohlfing, O. Guillon, Modelling electro-chemically induced stresses in all-solid-state batteries: screening electrolyte and cathode materials in composite cathodes, J. Mater. Chem. A 11 (2023) 18801–18810, https://doi.org/10.1039/d3ta01729j.

[50] A. Jain, G. Hautier, C.J. Moore, S. Ping Ong, C.C. Fischer, T. Mueller, K.A. Persson, G. Ceder, A high-throughput infrastructure for density functional theory calculations, Comp. Mater. Sci. 50 (2011) 2295–2310, https://doi.org/10.1016/j.commatsci.2011.02.023.